Review of Scientific Instruments

RESEARCH ARTICLE | JULY 18 2024

Determination of the dynamic Young's modulus of quantum materials in piezoactuator-driven uniaxial pressure cells using a low-frequency AC method

Caitlin I. O'Neil ; Zhenhai Hu; Naoki Kikugawa ; Dmitry A. Sokolov; Andrew P. Mackenzie; Hilary M. L. Noad ; Elena Gati

Rev. Sci. Instrum. 95, 073909 (2024)
https://doi.org/10.1063/5.0210777

Review of Scientific Instruments ARTICLE pubs.aip.org/aip/rsi

Determination of the dynamic Young's modulus of quantum materials in piezoactuator-driven uniaxial pressure cells using a low-frequency AC method

Cite as: Rev. Sci. Instrum. 95, 073909 (2024); doi: 10.1063/5.0210777
Submitted: 27 March 2024 • Accepted: 19 June 2024 •
Published Online: 18 July 2024

Caitlin I. O'Neil,[1,2,a] Zhenhai Hu,[1,2] Naoki Kikugawa,[3] Dmitry A. Sokolov,[1] Andrew P. Mackenzie,[1,2] Hilary M. L. Noad,[1] and Elena Gati[1,b]

AFFILIATIONS

[1] Max Planck Institute for Chemical Physics of Solids, 01187 Dresden, Germany
[2] Scottish Universities Physics Alliance, School of Physics and Astronomy, University of St Andrews, St Andrews KY16 9SS, United Kingdom
[3] National Institute for Materials Science, Tsukuba, Ibaraki 305-0003, Japan

[a] caitlin.oneil@cpfs.mpg.de
[b] **Author to whom correspondence should be addressed:** elena.gati@cpfs.mpg.de

ABSTRACT

We report on a new technique for measuring the dynamic Young's modulus, E, of quantum materials at low temperatures as a function of static tuning strain, ϵ, in piezoactuator-driven pressure cells. In addition to a static tuning of stress and strain, we apply a small-amplitude, finite-frequency AC ($1\ \text{Hz} \lesssim \omega \lesssim 1000\ \text{Hz}$) uniaxial stress, σ_{ac}, to the sample and measure the resulting AC strain, ϵ_{ac}, using a capacitive sensor to obtain the associated modulus E. We demonstrate the performance of the new technique through proof-of-principle experiments on the unconventional superconductor Sr_2RuO_4, which is known for its rich temperature–strain phase diagram. In particular, we show that the magnitude of E, measured using this AC technique at low frequencies, exhibits a pronounced nonlinear elasticity, which is in very good agreement with previous Young's modulus measurements on Sr_2RuO_4 under [1 0 0] strain using a DC method [Noad *et al.*, Science **382**, 447–450 (2023)]. By combining the new AC Young's modulus measurements with AC elastocaloric measurements in a single measurement, we demonstrate that these AC techniques are powerful in detecting small anomalies in the elastic properties of quantum materials. Finally, using the case of Sr_2RuO_4 as an example, we demonstrate how the imaginary component of the modulus can provide additional information about the nature of ordered phases.

I. INTRODUCTION

Recent years have witnessed a surge in the study of the elastic properties of quantum materials, driven by the discovery of novel collective electronic phases that exhibit a strong coupling to the underlying crystal lattice. A prominent example is the observation of nematicity in a number of unconventional superconductors.[1,2] Here, measurements of the elastic constants have revealed a huge lattice softening,[3] which has served as a unique experimental fingerprint of nematic fluctuations.

Similarly, the strong coupling of electronic and lattice degrees of freedom makes such electronic systems particularly susceptible to tuning by physical pressure. Driven by novel developments in pressure-cell technology for tuning quantum materials by hydrostatic and uniaxial pressure,[4,5] important discoveries have been made in the field of quantum materials. Since the application of pressure does not introduce additional disorder into the system, pressure tuning has been instrumental in exploring the fundamental properties of quantum materials, such as superconducting T_c, in clean systems.[6]

As a result, the combination of the two—the ability to measure elastic properties while tuning the physical pressure—has proven to be a powerful addition to the toolbox for studying quantum materials. Recently, measurements of the lattice elasticity as a function of pressure have led to important insights into the fundamental question of the role of the lattice in electronic matter[7–9] and the identification of possible functionalities.[10] For example, in correlated quantum materials subjected to pressure tuning, nonlinear elastic behavior has been observed. This experimental observation was taken as a strong indication that the lattice profoundly affects the properties of the electronic system and vice versa. Notable experimental examples in this respect include the observation of the breakdown of Hooke's law[11,12] around the finite-temperature critical endpoint of the Mott metal–insulator transition in an organic conductor. A huge lattice softening has also been observed[13] at the pressure-induced electronic Lifshitz transition[14] in Sr_2RuO_4.

The conclusions above were obtained from measurements of stress–strain relationships under continuously tuned pressure,[4,5,15–17] e.g., in piezoactuator-driven pressure cells,[5] performed in the demanding cryogenic environment required for the study of quantum materials. These measurements were made possible by several recent advances in measuring both the applied stress, σ, and the resulting strain, ϵ, with high precision. In general, stresses and strains are tensor quantities (σ_{ij} and ϵ_{kl}) and are related by the compliance matrix S_{ijkl} (or the inverse elastic constant matrix C_{ijkl}), i.e., $\sigma_{ij} = \sum_{k,l} S_{ijkl}\epsilon_{kl}$. When stress, σ, is applied along a specific direction and the deformation, ϵ, is measured along the same direction, $i = j = k = l$, and the corresponding modulus, S_{iiii} (or S_{ii} in Voigt notation),[18] is the Young's modulus, which we denote as E throughout this paper. It is obtained experimentally from the measured stress–strain relationships via

$$E = \frac{d\sigma_{ii}}{d\epsilon_{ii}}. \tag{1}$$

E remains unchanged with ϵ in linear elastic systems, i.e., in systems that obey Hooke's law of elasticity. In contrast, the hallmark of nonlinear elastic systems is that E varies with strain.[11,13]

In this paper, we introduce a new method to measure $E(\epsilon)$ in piezoactuator-driven uniaxial pressure cells. In our new approach, we make use of low-frequency AC stresses and strains[19,20] to determine the AC Young's modulus. In fact, at ambient pressure, so-called Dynamical Mechanical Analyzer (DMA) spectroscopy measurements, in which the real and imaginary elastic moduli, E' and E'', are determined by the application of low-frequency, low-amplitude forces and measurements of the resulting strains (see Fig. 1), are well-established (see, e.g., Ref. 21). In general, as shown schematically in Fig. 1, a sinusoidal AC stress, $\sigma_{ac}(t) = \sigma_{ac,0}\sin(\omega_p t)$, induces an AC strain response, $\epsilon_{ac}(t) = \epsilon_{ac,0}\sin(\omega_p t - \delta)$, with a phase lag, δ. δ can take different values (see Fig. 1): for purely elastic behavior, an instantaneous strain response is expected ($\delta = 0°$ and $E' \neq 0, E'' = 0$), whereas liquids are characterized by a purely viscous behavior with $\delta = 90°$ and $E' = 0, E'' \neq 0$. When δ takes values between 0° and 90°, the stress–strain response is classified as viscoelastic, and both E' and E'' are finite. These DMA methods are used intensively in the study of viscoelastic properties[22,23] of soft materials, tissues, biomaterials, or polymers, e.g., to extract characteristic energies of glassy

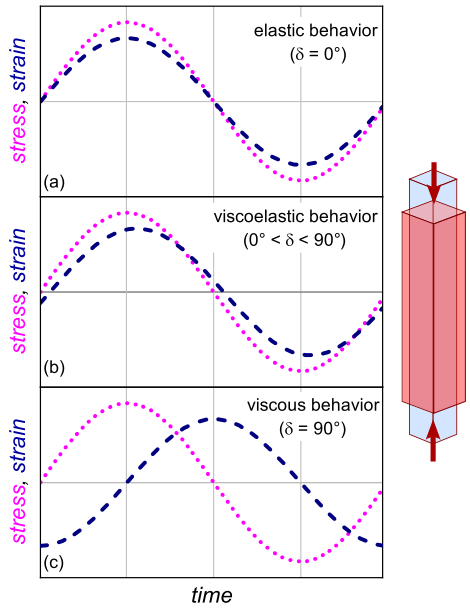

FIG. 1. Schematic representation of a dynamic elastic modulus measurement. An AC stress (dotted line) is applied to a sample, and the resulting AC strain (dashed line) is measured. The phase difference, δ, between the applied stress and the measured strain characterizes the degree of viscous and elastic behavior. For (a) $\delta = 0°$ [(c) $\delta = 90°$], a system exhibits purely elastic (viscous) behavior. If $0° < \delta < 90°$, a material is viscoelastic, i.e., it shows an elastic response similar to that of solids and liquids simultaneously (b). Note that viscoelastic deformation is still fully recoverable, whereas plastic deformation is characterized by unrecoverable deformation.

freezing processes of structural entities. In the context of rigid solids, the study of the dynamic moduli, E' and E'', has mainly been employed to study ferroelastic phase transitions, where strain acts as the primary order parameter. From the frequency, amplitude, and temperature dependence of E' and E'', the contribution of microstructural changes to the macroscopic elastic Young's modulus has been deduced (e.g., due to domains). In this respect, the observation of superelasticity in ferroelastic materials was a particularly relevant discovery.[24–26] Here, the stress-induced movement of domain walls[25] triggers significant length changes and, thus, results in a large "superelastic" softening.

The new setup described in this paper combines the concepts of DMA measurements with the ability to precisely apply static tuning uniaxial pressures in piezoactuator-driven uniaxial pressure cells.[5,15] At the present time, these cells are widely used in the field of quantum materials because they are compatible with a low-temperature and high-magnetic field environment and allow for *in situ* DC and AC stress tuning.[5,19] In this context, DMA-type measurements are very promising to investigate, e.g., the character of phase transitions, the role of stress-induced domain dynamics,[27] or other collective effects.[28,29] In Sec. II, we first describe the experimental setup used for the dynamic Young's modulus measurements and the data analysis procedure. Then, we show in Sec. III our proof-of-principle experiments on Sr_2RuO_4, where we demonstrate that the magnitude of the Young's modulus obtained in our setup is in very good agreement with the previous literature results from a DC technique.[13] We

conclude the paper by discussing the experimental results of a finite imaginary part of the Young's modulus under high uniaxial compression in the magnetic phase of Sr_2RuO_4 as an illustration of the DMA-type analysis, which is now possible with our setup.

II. EXPERIMENTAL SETUP AND DATA ANALYSIS

A. The uniaxial pressure cell and determination of the static Young's modulus

We use a uniaxial pressure cell, which is shown schematically in Fig. 2 and is similar to the one described in Ref. 15, for *in situ* control of the pressure applied to the sample. Here, we briefly review the working principle of the pressure cell.

The cell uses piezoelectric actuators to apply the force to the sample. In the piezocartridge, three piezoelectric actuators are combined to either apply compressive or tensile forces to the sample, depending on the sign of the applied voltage. In the present design, the two outer actuators apply compression to the sample upon application of a positive voltage, whereas the inner one applies tension (see Fig. 1 of Ref. 15). Accordingly, we refer to the two actuators (one actuator) as compression (tension) stacks (stack) throughout the paper.

The piezoelectric actuators drive the motion of the moving block A (see Fig. 2), which is guided by flexures with a low longitudinal spring constant. This changes the size of the gap between blocks A and B. When a sample is mounted between these two blocks, it is either compressed or stretched. In the present case, we mount our sample on a sample carrier that connects between moving blocks A and B (details on the sample carrier design and implications for the data analysis will be provided in Sec. II D). The purpose of the sample carrier is to facilitate sample exchange (see, e.g., Ref. 30). A capacitive sensor is mounted below the gap between the moving blocks A and B to measure the relative displacement of the moving blocks, which is related to the sample strain.

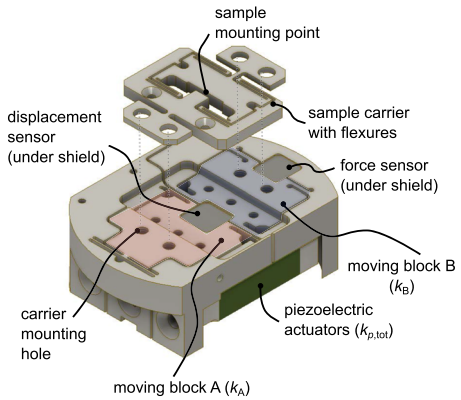

FIG. 2. Piezoactuator-controlled uniaxial pressure cell[15] used to measure the stress–strain relationship in quantum materials. In this cell, a set of piezoelectric actuators (green) generates a displacement across a gap between moving block A (highlighted in red) and moving block B (highlighted in blue). The sample carrier, on which the sample is mounted, connects A and B so that the displacement is transmitted to the sample. The displacement of the gap is measured by a capacitive sensor mounted under a shield. In addition, the cell houses a capacitive force sensor, which is used for DC stress–strain measurements. The cell's spring constant is determined by that of the moving blocks (k_A and k_B) as well as that of the actuators ($k_{P,tot}$).

The cell contains a second capacitive sensor that acts as a force sensor. The moving block B is connected to the frame of the cell by flexures having a larger longitudinal spring constant compared to the flexures of the moving block A (see Appendix A for details). The capacitor measures the displacement of these flexures, which can then be converted into the applied force using the known spring constant of these flexures.

The DC capacitances of the displacement and force sensors can be measured separately using high-precision capacitance bridges, such as the model AH2550A from the company Andeen–Hagerling. As described in detail in Ref. 13, these measurements, together with precise knowledge of the sample dimensions, can be used to calculate the applied stress, σ, and the resulting strain, ϵ, along the direction of the applied force. Taking the derivative of σ with respect to ϵ in the post-processing analysis then yields the Young's modulus, $E(\epsilon)$; see Eq. (1). Since these measurements are based on static measurements of σ and ϵ, we will refer to them throughout the text as *static* Young's modulus measurements, or, in short, the DC method.

B. Working curve of the piezoactuator-driven stress cell

The working principle of our new AC technique is based on the fact that piezoelectric actuators themselves can be used to measure the spring constant of the spring on which they exert force, called the "load spring." This capability is rooted in their characteristic working curve,[15] where key working parameters of piezoelectric actuators, such as the supplied force and the created displacement, depend on the spring constant of the load spring.

In Fig. 3(a), we show a simplified version of our experimental setup to illustrate the concept. The cell with spring constant k_{cell}, which contains the piezoelectric actuators, pushes against a load spring with spring constant k_{meas}. k_{meas} is the key quantity that is to be determined in the experiment, which can be converted to the Young's modulus, E, of the sample. The working curve of the cell is determined by k_{cell} and is shown by the brown line in Fig. 3(b). At no load, i.e., $k_{meas} = 0$, the cell provides a large displacement, $\Delta d_{dc,0}$, at essentially no force for a given, fixed piezoactuator voltage, V_{dc}. In the case of an infinitely stiff sample with $k_{meas} \to \infty$, the cell provides a maximum force of $F_0 = k_{cell}\Delta d_{dc,0}$ for the same V_{dc} but no displacement. Accordingly, the displacement, Δd_{dc}, which is generated by the cell and delivered to the load spring, is a function of k_{meas}. For illustration, we also include in Fig. 3(b) two stress–strain curves corresponding to two different load springs, $k_{meas,1}$ and $k_{meas,2} > k_{meas,1}$. The applied force (displacement) is greater (smaller) for $k_{meas,2}$ compared to $k_{meas,1}$. We note here that the linearity of the working curve for this specific type of cell, within the ranges of forces and displacements relevant to these experiments, has been previously experimentally verified in Ref. 15.

This simplified picture describes the working characteristic of a cell at a fixed piezoactuator voltage for different values of k_{meas}. In our experiment, we want to measure the changes in k_{meas} of a single sample with changing stress and strain, which is achieved by varying the static voltage on the piezoelectric actuator.

In particular, we are interested in obtaining the dynamic moduli from an AC experiment. To this end, we apply a small AC voltage to the piezoelectric actuators, which creates oscillating stresses and strains. Whereas the AC component serves to *probe* the Young's modulus, we use the DC voltages on the piezoelectric actuators to

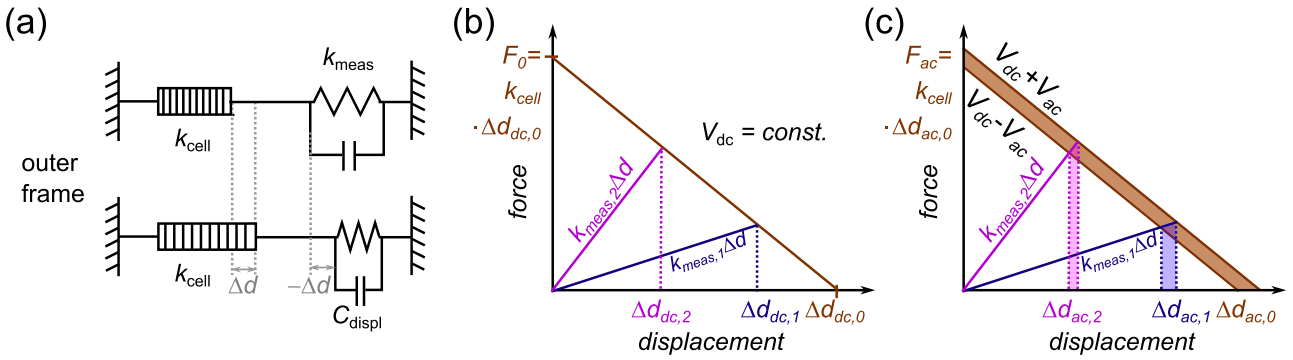

FIG. 3. (a) Simplified schematic diagram of the uniaxial pressure cell and its working principle. The cell with spring constant k_{cell} applies varying forces to the "load" spring k_{meas}, whose magnitude is to be determined in the experiment (see the text for details). The displacement of the load spring, Δd, can be measured by a capacitive displacement sensor, and its magnitude is identical to the displacement created by the cell. (b) Working curve of applied force, F, vs generated displacement, Δd_{dc}, of the piezoactuator-driven uniaxial pressure cell at a constant supply voltage on the piezoelectric actuators, V_{dc}. The working curve is determined by the parameters k_{cell}, the maximum displacement at this V_{dc} without a load, $\Delta d_{dc,0}$, and the maximum generated force, F_0, in the case of an infinite load. It is shown by the brown line following the form $F = F_0 - k_{cell}\Delta d_{dc}$. The magnitude of the load spring constant, k_{meas}, determines the force/displacement provided by the cell at this particular voltage, as seen from the working curve. This is illustrated by showing two linear stress–strain relationships, corresponding to two different values of k_{meas}. The intersection of these stress–strain relationships with the working curve determines the applied force and created displacement. The larger k_{meas}, the smaller (larger) the created displacement (applied force) will be. (c) Working curve of the piezoactuator-driven uniaxial pressure cell when an AC voltage, V_{ac}, is applied in addition to the DC voltage, V_{dc}. The working range is now delineated by the two working curves at $V_{dc} \pm V_{ac}$. The alternating V_{ac} causes an alternating displacement, $\Delta d_{ac,0}$, created at zero force. The alternating displacement, Δd_{ac}, induced by V_{ac} at a finite load spring constant, k_{meas}, is related to the magnitude of k_{meas}; see the text for details.

tune a given material. The extended working curve illustrating the situation in our experiment is shown in Fig. 3(c). The working range of the cell in the presence of an AC voltage, V_{ac}, is now delineated by two parallel lines, corresponding to the working curves at $V_{dc} \pm V_{ac}$ (see brown area). In analogy to the previous discussion, the AC displacement is given by $\Delta d_{ac,0}$, when $k_{meas} = 0$, and will be zero when $k_{meas} \to \infty$. Consequently, Δd_{ac} is directly related to k_{meas} for the constant amplitude of V_{ac}. In particular, the larger k_{meas}, the smaller Δd_{ac} will be. Since the AC voltage is used to measure k_{meas}, the DC voltage can be used independently to tune the elastic properties of the material under investigation.

C. Electronic setup for determining the dynamic Young's modulus using the new AC method

Thus, to directly measure k_{meas}, our technique relies on the accurate determination of Δd_{ac}, which is a mechanical modulation induced by a finite piezoactuator voltage V_{ac}, through a capacitive measurement. To this end, we have designed a home-built capacitance bridge that allows Δd_{ac} to be measured simultaneously with Δd_{dc} from a single displacement capacitor. The ability to measure both is important to determine the probing strain (related to Δd_{ac}) separately from the tuning strain (related to Δd_{dc}).

The detailed working principle of the bridge is shown in Fig. 4. A small AC voltage is superimposed on the DC voltage of one of the stacks. In our case, the voltage on the compression stacks is superimposed by an AC modulation with a frequency of ω_p, i.e., $V(t) = V_{dc} + V_{ac}\sin(\omega_p t)$. This, in turn, induces a mechanical displacement of the gap, which is measured through a capacitive displacement sensor with capacitance C_{displ}. The distance of the capacitor plates then follows the form $d = d_{dc} + \Delta d_{ac}\sin(\omega_p t + \delta)$, with $d_{dc} = d_{dc,0} + \Delta d_{dc}$ and $d_{dc,0}$ the initial distance of the capacitor plate. Accordingly, the time dependence of C_{displ} follows as $C_{displ} = C_{dc} + C_{ac}\sin(\omega_p t + \delta)$. In the first approximation, if $\Delta d_{ac} \ll d_{dc}$, these capacitances are related to the displacements by

$$\frac{\Delta d_{ac}}{d_{dc}} = \frac{C_{ac}}{C_{dc}}. \tag{2}$$

To extract C_{ac} and C_{dc} from C_{displ}, we use a circuit consisting of a voltage source operating at a second frequency, ω_c, and two lock-in amplifiers from Stanford Research Systems: in particular, a SR830 model and a SR860 model (see Fig. 4). In general, applying an AC voltage with a frequency of ω_c to a capacitor with a time-independent value of C_{dc} generates an AC current with a frequency of ω_c. In our present case, where C_{displ} is time-dependent, the returned current, with a characteristic frequency of ω_c, will be further modulated by ω_p. This modulated current is passed through a resistor with R_c, where it produces a voltage, V_R, which reads as

$$V_R = C_{dc}V_0R_c\omega_c\cos(\omega_c t) + C_{ac}V_0R_c \times[\omega_c\cos(\omega_c t)\sin(\omega_p t + \delta) + \omega_p\cos(\omega_p t + \delta)\sin(\omega_c t)], \tag{3}$$

see Appendix B for details. The main task of the two lock-in setups is to perform an electrical demodulation of the signal.[31] The first term is directly proportional to C_{dc} and, thus, to d_{dc}. It corresponds to the high-frequency signal represented by the blue curve in Fig. 4 (for $\omega_c \gg \omega_p$). We read out this component of the voltage in Eq. (3) by locking the SR830 to ω_c, such that $V_{SR830} = C_{dc}V_0R_c\omega_c$. The second and third terms in Eq. (3) are products of waves with the characteristic side-band frequencies $|\omega_c \pm \omega_p|$ (see also the red line in the Fourier transform in Fig. 4). To read out these voltages, we use the SR860 in dual reference mode, which measures the voltage at the frequency $|\omega_c - \omega_p|$. It then follows that

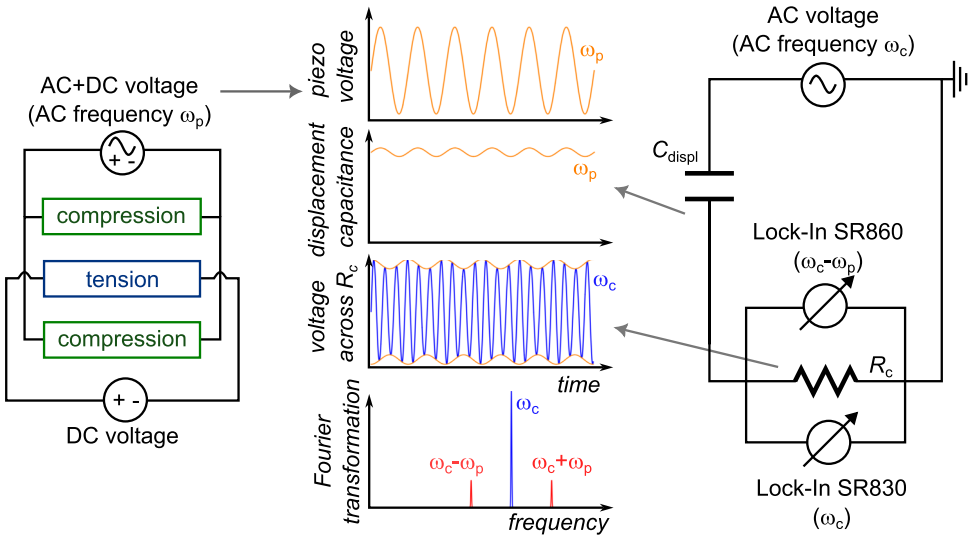

FIG. 4. Electronic setup for determining the AC displacement, Δd_{ac}, which is related to the sample Young's modulus. The piezocartridge, which drives the uniaxial pressure cell, consists of two compression stacks and one tension stack. A DC voltage is applied to all stacks to control the static uniaxial pressure on the sample. The DC voltage on the compression stacks is superimposed by a small AC voltage with a frequency of ω_p. The AC modulation of the voltages on the compression stack results in an AC change in the capacitance of the displacement sensor, $C_{displ}(t) = C_{dc} + C_{ac}(t)$, with the same frequency of ω_p. To measure the contributions of C_{dc} and C_{ac} to C_{displ} independently, a home-built capacitance bridge consisting of an AC voltage supply with a frequency of ω_c, a resistance of R_c, and two lock-in amplifiers (Stanford Research SR860 and SR830) is used. The voltage across the resistor (blue line) corresponds to the modulated signal of signals with frequencies of ω_p and ω_c (see the orange enveloping curve). As a result, as shown in the Fourier transformation of the voltage signal, the signal is composed of signals at ω_c (blue line) as well as at $|\omega_c \pm \omega_p|$ (red line). The SR830 reads out the component of the voltage signal at ω_c, which is related to the DC capacitance value (blue line), whereas the SR860 in dual reference mode picks up the signal at the beat frequency $\omega_c - \omega_p$, which is proportional to the AC capacitance; see the text for details. The input reference signal for the SR830 is taken from the AC voltage source and has a frequency of ω_c. The same reference signal is also used for the SR860 in dual reference mode, in addition to the second reference signal with ω_p, which is taken from the AC driving source of the piezoelectric actuators.

$$V_{SR860} = \frac{C_{ac} V_0 R_c |\omega_c - \omega_p|}{2}, \tag{4}$$

which can be directly converted to C_{ac}. The signal-to-noise ratio of V_{SR860} will be larger, the greater the difference between ω_p and ω_c.

Using the known calibration of the displacement sensor, i.e., the functional form of C_{displ} vs d, Δd_{ac}, and Δd_{dc} can now be calculated from the measured voltages V_{SR830} and V_{SR860}. In Fig. 5(a), we show an example curve of Δd_{ac} vs tuning displacement, Δd_{dc}, taken on Sr_2RuO_4. We will discuss the implications of the data in detail below in Sec. III. For now, the plot clearly shows that Δd_{ac} is not constant when Δd_{dc} is changed, and that the changes in Δd_{ac} can be clearly resolved in our setup with a resolution of ≈0.2 nm. As explained above, the changing Δd_{ac} reflects the changing k_{meas} (or, in other words, the changing Young's modulus, E, of the sample).

As an aside, we would like to remark that the precise determination of Δd_{ac} and hence ϵ_{ac}, which we demonstrate here, is also crucial for quantitative measurements of the elastocaloric effect,[19,20] where the temperature change, ΔT, induced by a finite ϵ_{ac}, is measured.

D. Data analysis

We now discuss how to convert the measured $\Delta d_{ac}(\Delta d_{dc})$ into absolute values of the Young's modulus $E(\epsilon)$. This requires two main steps: (i) converting Δd_{ac} to the measured spring constant, k_{meas}; and (ii) extracting the sample's spring constant from k_{meas}. This second step is necessary because k_{meas} contains contributions from, e.g., the mounting glue and the sample carrier, in addition to the contribution of the sample. This part of the analysis is also required when analyzing the data from the DC method and is described in detail in the supplementary material in Ref. 13.

For the first step, we refer back to the working curve of the cell, which has been introduced in Sec. II C and is shown in Fig. 3(c). For example, we can compare the AC displacement in the case of an empty cell, $\Delta d_{ac,0}$, with the displacement, Δd_{ac}, when the cell works against a load spring with k_{meas}. Clearly, $\Delta d_{ac} < \Delta d_{ac,0}$ and it can be deduced that the ratio determines k_{meas} via

$$k_{meas} = k_{cell}\left(\frac{\Delta d_{ac,0}}{\Delta d_{ac}} - 1\right). \tag{5}$$

Thus, k_{meas} can be calculated for all values of Δd_{ac} when $\Delta d_{ac,0}$ is measured, e.g., when the sample is broken after an experiment. Alternatively, any reference point with finite k_{meas} can be chosen, as long as the value of k_{meas} at a particular strain is well known.

The key parameter for converting Δd_{ac} to k_{meas} is the value of the cell spring constant, k_{cell}, which cannot be determined during the experiment itself. In general, it can be determined from calibration experiments and simulations, as shown in Ref. 15 for a cell of similar design. Following the same procedure, we determined the cell spring constant of the present cell to be $k_{cell} = (3.4 \pm 0.5)$ N/μm (see Appendix A for details). Since the titanium, the material of the cell, becomes stiffer upon cooling and calibration experiments were performed at room temperature, we applied a correction factor of

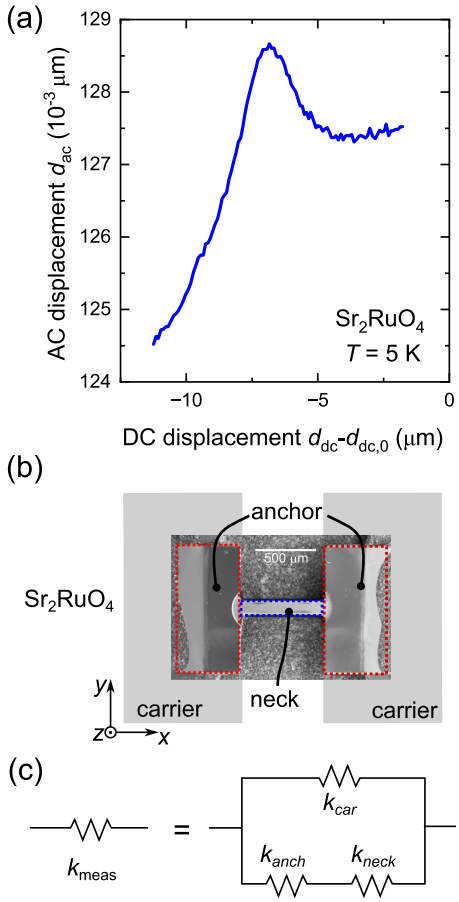

FIG. 5. (a) Experimental data of the AC displacement, Δd_{ac}, as a function of the DC tuning displacement, Δd_{dc}, induced by the application of a DC and an AC voltage on the piezoelectric actuators. d_{ac} and d_{dc} were obtained by reading out the displacement capacitive sensor in the piezoactuator-driven pressure cell with our home-built capacitance bridge. This example dataset was recorded on Sr_2RuO_4 at a temperature of T = 5 K, a frequency f_p of 167 Hz, and an AC amplitude V_{ac} of 5 V. (b) Preparation and mounting of samples for stress–strain measurements in uniaxial pressure cells. The sample (in the present case, Sr_2RuO_4) is cut into a narrow neck with wide anchor tabs using a plasma focused ion beam. The anchors are epoxied to the sample carrier. The sample shape ensures a rapid crossover from the low-stress region in the anchor tabs to the high-stress region in the neck and minimizes the stress in the mounting epoxy. (c) Due to the shape of the sample, the sample's spring constant can be modeled to a good approximation as a set of two discrete springs in series, i.e., the anchor (spring constant k_{anch}) and the neck spring (spring constant k_{neck}). In addition, the small carrier spring constant, k_{car}, contributes to the measured spring constant, k_{meas}, and is in parallel to the k_{anch} and k_{neck}.

15% to k_{cell} when analyzing low-temperature data.[15] The exact value of k_{cell} will likely vary from cell to cell, even if the design is technically the same. Once k_{cell} is determined for a specific cell, e.g., by calibration measurements, it is not expected to change from experiment to experiment and is, thus, not a free parameter in the analysis. Equation (5) also shows that the ability to resolve changes in k_{meas} also depends on k_{cell}. As expected from the working curve, the setup works best when k_{cell} and k_{meas} are of similar magnitude.

The second step in obtaining $E(\epsilon)$ from the AC data is to extract the spring constant of the sample from k_{meas}. Following the protocol established in Ref. 13, the samples are cut into a narrow neck with wide anchor tabs using a Xe plasma focused ion beam [see Fig. 5(b)]. The necking creates a rapid crossover between regions of low stress in the anchors and high stress in the neck. The sample can, therefore, be approximated by two springs in series, which we label as k_{neck} and k_{anch}. We also include the spring constant of the mounting glue in k_{anch}. In the two-spring approximation, k_{anch} can be calculated from the total measured signal k_{meas} around a reference strain and an independently measured value of E at that reference strain.[13] The independently measured value of E can, e.g., be obtained from ultrasonic experiments.[32] In the case of Sr_2RuO_4 over the range of displacements considered here, Ref. 13 shows that k_{anch} can indeed be taken as stress-independent to a good approximation.

In addition, the sample carrier has flexures with spring constants k_{car}, which are in series with k_{neck} and k_{anch}, as shown schematically in Fig. 5(c). Consequently,

$$k_{neck}(\epsilon) = \left[\frac{1}{k_{meas}(\epsilon) - k_{car}} - \frac{1}{k_{anch}}\right]^{-1}. \quad (6)$$

The spring constant of the carrier, $k_{car} \approx 0.02$ N/μm, is per design much smaller than typical values of k_{meas} and can also be calibrated experimentally.

Finally, the Young's modulus is obtained from an exact knowledge of the length of the necked region, l_{neck}, and the cross-sectional area of the sample, A_{cs}, via $E = k_{neck} l_{neck}/A_{cs}$. The strain in the neck, ϵ_{xx}, follows from the measured d_{dc} values via $(k_{meas}/k_{neck}) \times (\Delta d_{dc}/l_{neck})$. The sample of Sr_2RuO_4 used for our proof-of-principle measurements shown in Fig. 5(b) was cut to dimensions of A_{cs} = 102 ×120 μm^2 and l_{neck} = 717 μm, with the long edge of the neck oriented along the x = [1 0 0] direction of the crystal, so that $k_{neck}(\epsilon_{xx} = 0) = 2.72$ N/μm. The anchor spring constant in our experiments was $k_{anch} = 2.36$ N/μm.

E. Working parameters of the AC Young's modulus setup

In the following, we specify the working range of the AC Young's modulus setup, including accessible frequency, amplitude, and temperature range.

The frequency range of operation is determined by the choice of piezoelectric actuators and the mechanical resonances of the cell. The multi-layer ceramic actuators[33] typically used in the pressure cells operate well in the low-frequency range of 1 Hz $\lesssim f_p = \omega_p/(2\pi) \lesssim$ 1 kHz. Future technical developments might be able to extend the frequency range significantly, e.g., by choosing different types of actuators.

The second relevant frequency is that of the capacitance bridge, f_c. All measurements in this paper were taken with $f_c = \omega_c/(2\pi)$ = 2.297 kHz, which is of the same magnitude as the frequency of 1 kHz used in the Andeen–Hagerling AH2550A capacitance bridges, employed in the earlier DC work.

In terms of amplitude, the maximum voltage that can be applied to the actuators is temperature dependent. At the lowest temperatures, the voltage range can typically be extended[15] to $-300 \le V_{dc} \le 400$ V. With such large DC voltages, tuning strains of

±1%–2% may be achieved for a sample of the previously mentioned dimensions. Since the AC voltage produces the probing strain, its magnitude must be chosen to be much smaller than the DC voltages. In our proof-of-principle studies on Sr_2RuO_4, we used AC voltages, V_{ac}, up to 5 V at the lowest temperatures, corresponding to typical values of stress and strain amplitude of $\sigma_{ac} \approx 10^{-2}$ GPa and $\epsilon_{ac} \approx 1 \times 10^{-4}$. V_{ac} and f_p were chosen to optimize the signal-to-noise ratio while ensuring that phase transition features were not significantly smeared out by a large V_{ac}. The smallest capacitance that we can resolve with our bridge is estimated to be around 5×10^{-6} pF, corresponding to 0.2 nm, for our specific displacement capacitor. In the case of the Sr_2RuO_4 sample used in this study and the specific cell, this translates into a resolution of the Young's modulus of 0.1 GPa.

The piezoactuator-driven uniaxial pressure cells are designed to operate down to very low temperatures, even down to dilution-fridge temperatures. Typically, the lowest-accessible temperature is limited by the cooling power of the fridge and by the heating created by the piezoelectric actuators. In the AC setup, heating of the actuators becomes a serious problem at higher frequencies and/or higher AC voltage amplitudes. Thus, in practical terms, the lowest accessible temperature may be a trade-off with the frequency/amplitude range of interest.

The AC Young's modulus measurements can also be performed in a finite magnetic field, which then allows the simultaneous study of the effect of different tuning parameters on the elastic properties of quantum materials.

III. PROOF-OF-PRINCIPLE RESULTS

To demonstrate the functionality of our new AC Young's modulus setup, we performed proof-of-principle experiments on the ruthenate Sr_2RuO_4, whose Young's modulus under finite strain has recently been documented with high precision by DC stress–strain measurements.[13] Before discussing our proof-of-principle AC data taken on Sr_2RuO_4, we first present the main aspects of the phase diagram of Sr_2RuO_4 under uniaxial pressure that are relevant to the present work.

The unconventional superconductor Sr_2RuO_4 has been extensively studied in uniaxial pressure experiments[6,13,14,20,30,34] in the last decade. These studies have uncovered a rich phase diagram under uniaxial stress, σ_{xx}, applied along the [1 0 0] axis of the tetragonal lattice. Upon increasing compression, the Fermi surface of Sr_2RuO_4, consisting of so-called α, β, and γ sheets (see sketches on top of Fig. 6), becomes distorted. The γ sheet shows the strongest changes. When a compressive [1 0 0] strain of $\epsilon_{xx} \approx -0.45\%$ is applied, the γ sheet undergoes a Lifshitz transition, at which the Fermi surface drastically changes its topology[14] from a closed to an open configuration. Although the Lifshitz transition involves only a fraction of the conduction electrons, it has recently been shown by Noad *et al.*[13] that these conduction electrons drive a very large lattice softening. The significant renormalization of the Young's modulus upon crossing the Lifshitz transition, which is reported with high accuracy, provides an excellent testbed to benchmark our new AC method. In addition, a recent set of experiments,[20,34] including thermodynamic measurements of the elastocaloric effect, suggests that Sr_2RuO_4 undergoes a transition into a magnetically ordered state for higher compression beyond the Lifshitz strain and temperatures

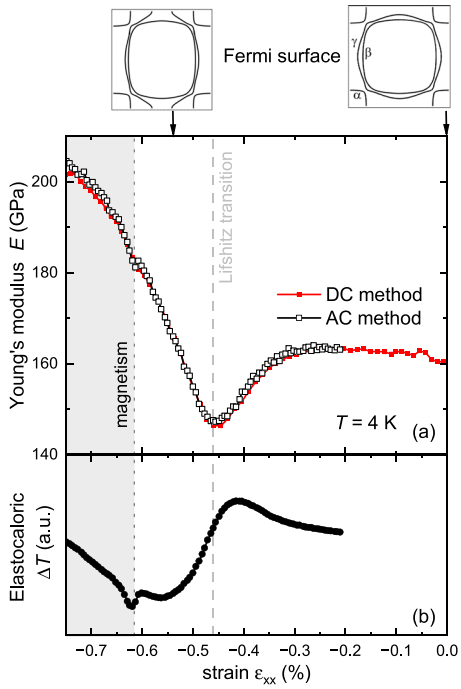

FIG. 6. (a) Young's modulus, E, of Sr_2RuO_4 as a function of strain, ϵ_{xx}, at a temperature of $T = 4$ K, extracted from the new AC method (open symbols) and compared to results from the DC method (closed symbols) on the same sample. The data in the AC method was taken at a frequency of $f_p = 167$ Hz and a piezoactuator AC voltage of $V_{ac} = 5$ V. (b) Elastocaloric temperature oscillation amplitude, ΔT, measured in the same experiment as the Young's modulus data shown in (a). In both panels, the dashed line indicates the strain at which Sr_2RuO_4 undergoes a Lifshitz transition of the Fermi surface, which is schematically shown in the insets. The dotted line indicates the strain at which Sr_2RuO_4 undergoes a transition to magnetic order.

$T \lesssim 8$ K. This additional phase transition is expected to lead to anomalous behavior in $E(\epsilon_{xx})$.

In the following, we first discuss the results of the magnitude of the dynamic Young's modulus of Sr_2RuO_4. For low-enough frequencies, it may be expected that the magnitude of the AC Young's modulus agrees with the one inferred from DC measurements. Afterward, we discuss our measurements of the phase shift in the dynamic signal as we tune the material into its magnetically ordered regime.

A. Results: Magnitude of the dynamic Young's modulus of Sr_2RuO_4, determined from the AC technique

In Fig. 6(a), we compare the results of Young's modulus measurements conducted at a temperature of 4 K with the DC method[13] (closed symbols) vs the new AC method (open symbols), taken on the exact same sample of Sr_2RuO_4 in the same experimental run. Clearly, the two datasets as a function of tuning strain, ϵ_{xx}, are in very good agreement. The quantitative agreement is achieved by using $k_{cell} = (3.7 \times 1.15)$ N/μm in the analysis (see Sec. II D). This

value is within the error bars of the simulation results for k_{cell} (see Appendix A).

Importantly, the data show a set of anomalies associated with the rich phase diagram of Sr_2RuO_4 under [1 0 0] stress. The pronounced softening of E at the electronic Lifshitz transition at around −0.45% strain is clearly resolved. Upon further increasing compression, a second, although smaller, anomaly can be discerned in the $E(\epsilon_{xx})$ data around $\epsilon_{xx} \approx -0.64\%$. Although the anomaly is visible in both the DC and AC datasets, it is slightly more evident in the AC dataset. The fact that this small drop in $E(\epsilon_{xx})$ does indeed correspond to a thermodynamic phase transition becomes clear when comparing the results of elastocaloric measurements, which were performed simultaneously with the $E(\epsilon_{xx})$ measurements. The elastocaloric temperature amplitude, ΔT, manifests an anomaly at the same strain as where the small drop in E occurs. In the previous work by Li *et al.*,[20] this feature was associated with the transition into the magnetically ordered phase[34] of Sr_2RuO_4.

The AC Young's modulus data in Fig. 6 were taken at f_p = 167 Hz, f_c = 2.297 kHz, and V_{ac} = 5 V. In Fig. 7, we now show our data

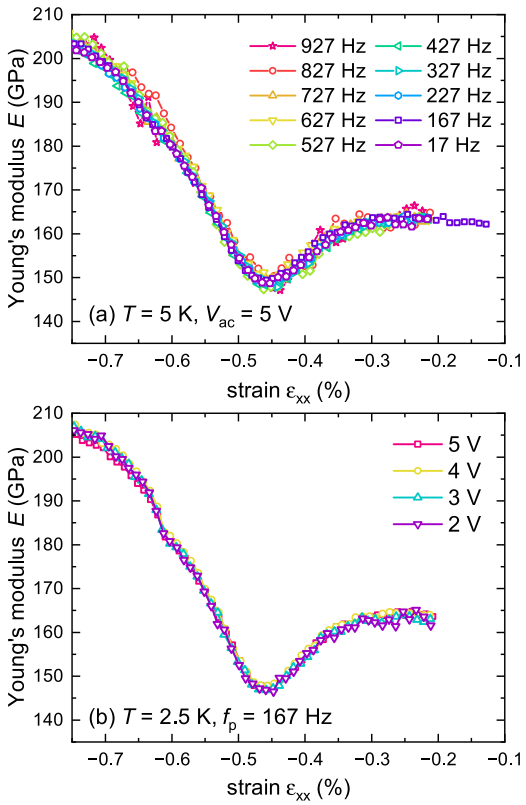

FIG. 7. Dependence of the Young's modulus, E, of Sr_2RuO_4 on frequency (a) and stress amplitude (b), as obtained by the new AC method. The data are plotted as a function of strain, ϵ_{xx}. In (a), different actuator frequencies, f_p, are applied in the range between 17 and 927 Hz at a temperature of 5 K and an AC voltage of 5 V. This voltage induces a stress amplitude of σ_{ac} = 0.027 GPa. In (b), the data for different AC voltage amplitudes, V_{ac}, between 2 and 5 V are shown at a temperature of 2 K and an actuator frequency of 167 Hz. The corresponding stress amplitudes, σ_{ac}, vary between 0.011 and 0.027 GPa. All data shown were taken with a capacitance-bridge frequency of f_c = 2.297 kHz.

at different f_p (a) and different V_{ac} (b) to demonstrate experimentally that our setup is operational over wider ranges of f_p and V_{ac}. Both datasets demonstrate that the magnitude of Young's modulus is essentially independent of the exact frequency or amplitude within the ranges of 17 Hz ≤ f_p ≤ 927 Hz and 2 V ≤ V_{ac} ≤ 5 V. In particular, in Fig. 7(a), the feature of the Lifshitz transition, which is the prominent feature at T = 5 K, is clearly visible in all datasets at different f_p, and the absolute value of E agrees between the datasets within the signal-to-noise ratio. However, the latter is smaller at higher frequencies, as expected, since the absolute signal depends on $\omega_c - \omega_p$, as shown in Eq. (4).

We now demonstrate that the chosen V_{ac} is small enough to not smear out phase transitions. To this end, we show in Fig. 7(b) the amplitude dependence of the Young's modulus at a temperature of 2.5 K, where the feature associated with the magnetic phase at $\epsilon_{xx} \sim -0.62\%$ is more pronounced and, thus, serves as a good benchmark for this analysis. For the range of V_{ac} between 2 and 5 V, corresponding to a range of σ_{ac} (ϵ_{ac}) between 0.011 and 0.027 GPa (6×10^{-5} and 1.5×10^{-4}), no significant smearing of Young's modulus anomalies can be detected. Overall, all the data agree quantitatively very well, and only the signal-to-noise ratio changes with decreasing V_{ac}, as expected.

B. Results: Phase of the dynamic Young's modulus of Sr_2RuO_4

We now turn to the additional phase information that is provided by performing our measurements in AC mode. As introduced in Sec. I, dynamic measurements reveal information on the real and imaginary parts of the Young's modulus (E' and E''). In particular, the latter is of interest in investigating dissipative processes. In the following, we describe our results in this respect by presenting the Young's modulus in terms of its magnitude and phase. Phase and magnitude are related to the real and imaginary parts of the modulus via $E' = \frac{|\sigma_{ac,0}|}{|\epsilon_{ac,0}|} \cos\delta$ and $E'' = \frac{|\sigma_{ac,0}|}{|\epsilon_{ac,0}|} \sin\delta$, i.e., a finite δ corresponds to a finite E''.

Figure 8 summarizes our measurement results of δ in our experiments on Sr_2RuO_4 at a probing frequency of f_p = 167 Hz and V_{ac} = 5 V. To this end, we now compare the results at two different temperatures, T = 2.5 K and T = 8 K. Whereas Sr_2RuO_4 was reported to enter a magnetically ordered phase at high compression at T = 2.5 K, it remains non-magnetic at 8 K.[20,34] This is fully consistent with our thermodynamic data, as shown in Fig. 8(a). At low compression, the magnitude of E as a function of ϵ_{xx} shows the softening at the Lifshitz transition, and the softening is more pronounced at low temperatures, consistent with the earlier reports.[13] For higher compression, the data taken at 2.5 K reveal an additional feature at $\epsilon_{xx} \approx -0.62\%$, associated with the transition into the magnetic state. In contrast, the dataset taken at 8 K shows no features of additional phase transitions besides the Lifshitz transition. The gray area in Fig. 8 marks the region of magnetic order at 2.5 K, as determined by the simultaneous measurements of E and the elastocaloric effect (see the gray line, right axis).

In Fig. 8(b), we show the behavior of the phase, δ, as a function of ϵ_{xx} for the same temperatures and at the same frequency. At 8 K, no change in δ with strain is observed within the signal-to-noise level over the entire strain range. In contrast, at 2.5 K, an increase in δ is

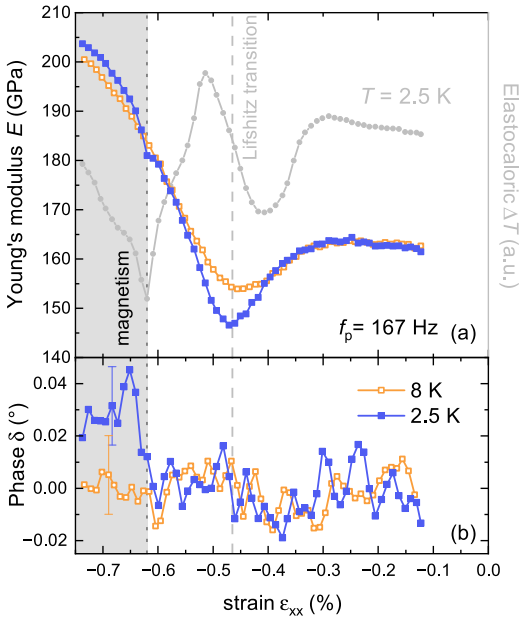

FIG. 8. Magnitude (a) and phase (b) of the dynamic Young's modulus of Sr_2RuO_4 under in-plane strain, ϵ_{xx}. Data on the dynamic modulus are shown at temperatures of 2.5 and 8 K. The strain region, in which Sr_2RuO_4 is magnetically ordered at 2.5 K, is indicated by the gray area. The transition into the magnetically ordered phase at 2.5 K and $\epsilon_{xx} \approx -0.62\%$ is also clearly identified in the elastocaloric temperature amplitude, ΔT, which is also included in (a) on the right axis. At 8 K, Sr_2RuO_4 remains non-magnetic over the strain range shown here.[20] The dashed line indicates the position of the Lifshitz transition at 2.5 K. All data shown were taken at a frequency of f_p = 167 Hz and an amplitude of V_{ac} = 5 V. Error bars for the phase value are exemplarily indicated in (b) at a strain of ~ −0.7%. Note that ΔT shows multiple features at 2.5 K, related to the strain-induced entry and exit into the superconducting state as well as the Lifshitz transition. No change of phase is observed across these transitions.

observed at the strain, where Sr_2RuO_4 undergoes the transition into the magnetically ordered state. Although the changes in δ are very small, they exceed the signal-to-noise ratio by more than a factor of two.

The result of a finite phase between applied stress and resulting strain in the magnetic phase of Sr_2RuO_4 is a key new insight accessible by extending stress–strain measurements to finite frequencies. It implies that there is energy dissipation during the (un-)loading stress cycle. Since this phenomenon occurs at low frequencies compared to typical spin relaxation times, it is likely to be related to interactions between the magnetic order and the crystal lattice, such as domain walls or other collective effects. In elemental chromium (Cr), for example, it was found that the pressure-dependent spin-density wave vector shows a certain degree of irreversibility between increasing and decreasing pressure.[35] This observation was interpreted in terms of crystal-lattice domain-wall distortions,[36] which lock the wave vector for small distortions. A similar mechanism may be at work here in Sr_2RuO_4. Further knowledge of the ordering vector and its strain dependence[37] in Sr_2RuO_4 will be crucial for understanding the low-frequency response of its elastic constants.

IV. CONCLUSION AND OUTLOOK

In this work, we describe a new experimental technique to determine the dynamic Young's modulus as a function of pressure, frequency, and temperature in piezoactuator-driven uniaxial pressure cells. Our setup exploits the ability of piezoelectric actuators to generate finite-frequency stresses and strains in the Hz–kHz range through the application of an AC voltage. Using the ruthenate Sr_2RuO_4 as a test-bed material for proof-of-principle measurements, we have shown that the Young's modulus data from our low-frequency AC setup is in very good agreement with data from static Young's modulus measurements. Our AC setup is well suited for detecting small anomalies in the strain dependence of the modulus. Furthermore, our AC data contains information on the phase between applied stress and resulting strain, which we find to be finite in the magnetic phase of Sr_2RuO_4 under high compression.

Our setup opens up the possibility of studying the finite-frequency elastic response function in quantum materials that are subjected to time-varying external stress fields and large, static tuning stresses. This approach is akin to AC susceptibility studies,[38,39] where a time-dependent magnetic field acts as the driving external force to probe dynamics. Our method provides a new perspective on the viscoelastic behavior and lattice dynamics of solids. Following the fluctuation–dissipation theorem,[40] the viscoelastic response is related to the low-frequency lattice dynamics of systems whenever they are amenable to stress tuning. It can be expected that the dynamics are governed by a range of intriguing phenomena, such as the movement of domain walls under strain, slow order-parameter dynamics, and collective effects in general. One of the many potentially interesting applications of this new approach is the study of the intrinsically low-frequency ($\lesssim$1 kHz) dynamics of frustrated magnets,[38] which may be tunable by uniaxial pressure.

ACKNOWLEDGMENTS

We thank You-Sheng Li and Clifford W. Hicks for highly useful insights from technical discussions. The financial support from the Max Planck Society is gratefully acknowledged. In addition, we gratefully acknowledge the funding through the Deutsche Forschungsgemeinschaft (DFG, German Research Foundation) through Grant No. TRR 288—422213477 (Project Nos. A10 and A13) and the SFB 1143 (Project-ID 247310070; Project No. C09). Research in Dresden benefits from the environment provided by the DFG Cluster of Excellence ct.qmat (EXC 2147, Project ID 390858490). C.I.O. and Z.H. acknowledge the support of a St. Leonards scholarship from the University of St. Andrews. N.K.'s work is supported by JSPS KAKENHI (Grant Nos. JP18K04715, JP21H01033, and JP22K19093).

AUTHOR DECLARATIONS

Conflict of Interest

The authors have no conflicts to disclose.

Author Contributions

Caitlin I. O'Neil: Data curation (equal); Formal analysis (equal); Investigation (equal); Methodology (equal); Writing – original draft (equal); Writing – review & editing (equal). **Zhenhai Hu**: Methodology (equal); Software (equal); Writing – review & editing (equal). **Naoki Kikugawa**: Resources (equal); Writing – review & editing (equal). **Dmitry A. Sokolov**: Resources (equal). **Andrew P. Mackenzie**: Conceptualization (equal); Funding acquisition (equal); Project administration (equal); Supervision (equal); Writing – review & editing (equal). **Hilary M. L. Noad**: Data curation (equal); Funding acquisition (equal); Investigation (equal); Supervision (equal); Visualization (equal); Writing – review & editing (equal). **Elena Gati**: Conceptualization (equal); Data curation (equal); Funding acquisition (equal); Methodology (equal); Supervision (equal); Visualization (equal); Writing – original draft (equal); Writing – review & editing (equal).

DATA AVAILABILITY

The data that support the findings of this study are openly available at https://doi.org/10.17617/3.FNC3P9.

APPENDIX A: DETERMINATION OF THE SPRING CONSTANT OF THE CELL

We follow the report of Barber *et al.*[15] to determine the spring constant of our cell, which is similar in design, but not identical, to theirs. For the finite-element simulations, we used the software COMSOL.[41] Since the cell is made out of titanium, we use the room-temperature Young's modulus of 103 GPa and a Poisson's ratio of 0.33 for the simulations.

The spring constant of the cell contains various contributions (see Fig. 2): (i) the spring constant of the piezoelectric actuators, $k_{p,tot}$; (ii) the spring constant of the moving block B (the force block), k_B; and (iii) the spring constant of the moving block A, k_A.

According to the data sheet of the actuators,[33] the spring constant of a single stack of type P-885.51 used here is $k_p = 50$ N/μm at room temperature. Combining the two compression actuators in parallel with each other and in series with the tension actuator gives $k_{p,tot} = 33$ N/μm.

To simulate k_B, we apply a force of 10 N to moving block B at the position of the carrier mounting holes and measure its displacement. The resulting longitudinal spring constant in the simulations was $k_B = (7.6 \pm 0.3)$ N/μm. We also determined this spring constant experimentally by hanging various weights from block B and measuring the resulting displacement. This procedure yielded an experimental value of (7.7 ± 0.1) N/μm, which is within the error bars and consistent with the simulated value.

The moving block A is designed to have a small spring constant in the direction of the applied force and a large spring constant in the orthogonal directions to avoid torque on the sample. These rotational spring constants are a factor of 40 larger than the longitudinal ones and, thus, dominate k_A. For the simulations of the rotational spring constant, we consider the application of a force of 10 N to an infinitely stiff sample. Since the sample is infinitely stiff, there is zero displacement between the carrier mounting points on blocks A and B ($\Delta d = 0$) upon the application of 10 N. Due to the finite rotational spring constant of block A, the actuators must apply a slightly higher force than 10 N. Our simulations showed that a force of 10.45 N is needed. We then evaluated the difference in actual displacement between the carrier mounting holes on block A and the actuator attachment area. Note that, even though there is zero relative displacement across the gap, block A is still displaced because block B moves under applied force (see Ref. 15 for further details on this simulation). The present simulation gives an estimate of the rotational spring constant to be $k_A = (7.7 \pm 2)$ N/μm.

Taking $k_{p,tot}$, k_A, and k_B together in series yields $k_{cell} = (3.4 \pm 0.5)$ N/μm at room temperature.

APPENDIX B: VOLTAGE SIGNAL DETECTED BY THE CAPACITANCE BRIDGE

In the following, we present the derivation for Eq. (3) in the main text. The application of the voltage $V(t) = V_{dc} + V_{ac}\sin(\omega_p t)$ induces an AC stress on the sample, which then induces an AC strain in the sample. As explained in the introduction, the induced AC strain can be phase-shifted with respect to the applied AC stress, and thus, the time dependence of the displacement capacitor reads as $C_{displ} = C_{dc} + C_{ac}\sin(\omega_p t + \delta)$. In the bridge setup in Fig. 4, an alternating voltage with different frequency ω_c is applied to the displacement capacitor, $V_C(t) = V_0\sin(\omega_c t)$. The current in the circuit, I, reads as

$$
\begin{aligned}
I &= \frac{dQ}{dt} = \frac{d\left(C_{displ}(t)V_C(t)\right)}{dt} \\
&= \omega_c C_{dc} V_0 \cos(\omega_c t) + C_{ac} V_0 [\omega_p \cos(\omega_p t + \delta)\sin(\omega_c t) \\
&\quad + \omega_c \sin(\omega_p t + \delta)\cos(\omega_c t)] \\
&= \omega_c C_{dc} V_0 \cos(\omega_c t) + \frac{1}{2} C_{ac} V_0 [(\omega_c - \omega_p)\sin((\omega_p - \omega_c)t + \delta) \\
&\quad + (\omega_c + \omega_p)\sin((\omega_c + \omega_p)t + \delta)].
\end{aligned}
$$

Since the SR860 in dual reference mode detects the signal at $|\omega_c \pm \omega_p|$, the magnitude of the voltage is given by Eq. (4), and the phase, δ, corresponds to the one between applied stress and resulting strain.

REFERENCES

[1] R. M. Fernandes, A. V. Chubukov, and J. Schmalian, Nat. Phys. **10**, 97 (2014).
[2] V. Hinkov, D. Haug, B. Fauqué, P. Bourges, Y. Sidis, A. Ivanov, C. Bernhard, C. T. Lin, and B. Keimer, Science **319**, 597 (2008).
[3] A. E. Böhmer, J.-H. Chu, S. Lederer, and M. Yi, Nat. Phys. **18**, 1412 (2022).
[4] E. Gati, L. Xiang, S. L. Bud'ko, and P. C. Canfield, Ann. Phys. **532**, 2000248 (2020).
[5] C. W. Hicks, M. E. Barber, S. D. Edkins, D. O. Brodsky, and A. P. Mackenzie, Rev. Sci. Instrum. **85**, 065003 (2014).
[6] A. Steppke, L. Zhao, M. E. Barber, T. Scaffidi, F. Jerzembeck, H. Rosner, A. S. Gibbs, Y. Maeno, S. H. Simon, A. P. Mackenzie, and C. W. Hicks, Science **355**, eaaf9398 (2017).
[7] M. Zacharias, I. Paul, and M. Garst, Phys. Rev. Lett. **115**, 025703 (2015).
[8] M. Zacharias, A. Rosch, and M. Garst, Eur. Phys. J. Spec. Top. **224**, 1021 (2015).
[9] S. Sarkar, L. Franke, N. Grivas, and M. Garst, Phys. Rev. B **108**, 235126 (2023).
[10] J. T. Sypek, H. Yu, K. J. Dusoe, G. Drachuck, H. Patel, A. M. Giroux, A. I. Goldman, A. Kreyssig, P. C. Canfield, S. L. Bud'ko, C. R. Weinberger, and S.-W. Lee, Nat. Commun. **8**, 1083 (2017).
[11] E. Gati, M. Garst, R. S. Manna, U. Tutsch, B. Wolf, L. Bartosch, H. Schubert, T. Sasaki, J. A. Schlueter, and M. Lang, Sci. Adv. **2**, e1601646 (2016).

[12]E. Gati, U. Tutsch, A. Naji, M. Garst, S. Köhler, H. Schubert, T. Sasaki, and M. Lang, Crystals **8**, 38 (2018).
[13]H. M. L. Noad, K. Ishida, Y.-S. Li, E. Gati, V. Stangier, N. Kikugawa, D. A. Sokolov, M. Nicklas, B. Kim, I. I. Mazin, M. Garst, J. Schmalian, A. P. Mackenzie, and C. W. Hicks, Science **382**, 447 (2023).
[14]V. Sunko, E. Abarca Morales, I. Markovic, M. E. Barber, D. Milosavljevic, F. Mazzola, D. A. Sokolov, N. Kikugawa, C. Cacho, P. Dudin, H. Rosner, C. W. Hicks, P. D. C. King, and A. P. Mackenzie, npj Quantum Mater. **4**, 46 (2019).
[15]M. E. Barber, A. Steppke, A. P. Mackenzie, and C. W. Hicks, Rev. Sci. Instrum. **90**, 023904 (2019).
[16]Y. Agarmani, S. Hartmann, J. Zimmermann, E. Gati, C. Delleske, U. Tutsch, B. Wolf, and M. Lang, Rev. Sci. Instrum. **93**, 113902 (2022).
[17]R. S. Manna, B. Wolf, M. de Souza, and M. Lang, Rev. Sci. Instrum. **83**, 085111 (2012).
[18]B. Lüthi, *Physical Acoustics in the Solid State*, *Springer Series in Solid-State Sciences*, 1st ed. (Springer, Berlin, Heidelberg, 2005), Vol. 148.
[19]M. S. Ikeda, J. A. W. Straquadine, A. T. Hristov, T. Worasaran, J. C. Palmstrom, M. Sorensen, P. Walmsley, and I. R. Fisher, Rev. Sci. Instrum. **90**, 083902 (2019).
[20]Y.-S. Li, M. Garst, J. Schmalian, S. Ghosh, N. Kikugawa, D. A. Sokolov, C. W. Hicks, F. Jerzembeck, M. S. Ikeda, Z. Hu, B. J. Ramshaw, A. W. Rost, M. Nicklas, and A. P. Mackenzie, Nature **607**, 276 (2022).
[21]E. K. H. Salje, W. Schranz, and Z. Kristallog, Z. Kristallogr. **226**, 1 (2011).
[22]S. Patra, P. M. Ajayan, and T. N. Narayanan, Oxford Open Mater. Sci. **1**, itaa001 (2020); https://academic.oup.com/ooms/article-pdf/1/1/itaa001/45723688/itaa001.pdf.
[23]T. Venkategowda, L. Manjunatha, and P. Anilkumar, "Dynamic mechanical behavior of natural fibers reinforced polymer matrix composites—A review," Mater. Today: Proc. **54**, 395 (2022).
[24]A. V. Kityk, W. Schranz, P. Sondergeld, D. Havlik, E. K. H. Salje, and J. F. Scott, Phys. Rev. B **61**, 946 (2000).
[25]W. Schranz and A. V. Kityk, Ferroelectrics **375**, 178 (2008).
[26]W. Schranz, H. Kabelka, A. Sarras, and M. Burock, Appl. Phys. Lett. **101**, 141913 (2012).
[27]W. Schranz, Phase Transitions **64**, 103 (1997).
[28]J. Müller, ChemPhysChem **12**, 1222 (2011).
[29]S. Wang, J. Chen, L. Wu, and Y. Zhao, Phys. Rev. Lett. **128**, 095702 (2022).
[30]F. Jerzembeck, H. S. Roising, A. Steppke, H. Rosner, D. A. Sokolov, N. Kikugawa, T. Scaffidi, S. H. Simon, A. P. Mackenzie, and C. W. Hicks, Nat. Commun. **13**, 4596 (2022).
[31]A. T. Hristov, J. C. Palmstrom, J. A. W. Straquadine, T. A. Merz, H. Y. Hwang, and I. R. Fisher, Rev. Sci. Instrum. **89**, 103901 (2018).
[32]S. Ghosh, A. Shekhter, F. Jerzembeck, N. Kikugawa, D. A. Sokolov, M. Brando, A. P. Mackenzie, C. W. Hicks, and B. J. Ramshaw, Nat. Phys. **17**, 199 (2021).
[33]Physik Instrumente, P-885.51 PICMA® Stack Multilayer Piezo Actuator.
[34]V. Grinenko, S. Ghosh, R. Sarkar, J.-C. Orain, A. Nikitin, M. Elender, D. Das, Z. Guguchia, F. Brückner, M. E. Barber, J. Park, N. Kikugawa, D. A. Sokolov, J. S. Bobowski, T. Miyoshi, Y. Maeno, A. P. Mackenzie, H. Luetkens, C. W. Hicks, and H.-H. Klauss, Nat. Phys. **17**, 748 (2021).
[35]D. W. Ruesink, J. M. Perz, and I. M. Templeton, Phys. Rev. Lett. **45**, 734 (1980).
[36]E. W. Fenton, Phys. Rev. Lett. **45**, 736 (1980).
[37]B. Kim, S. Khmelevskyi, C. Franchini, and I. I. Mazin, Phys. Rev. Lett. **130**, 026702 (2023).
[38]C. V. Topping and S. J. Blundell, J. Phys.: Condens. Matter **31**, 013001 (2018).
[39]S. A. Grigera, R. A. Borzi, A. P. Mackenzie, S. R. Julian, R. S. Perry, and Y. Maeno, Phys. Rev. B **67**, 214427 (2003).
[40]R. Kubo, Rep. Prog. Phys. **29**, 255 (1966).
[41]See http://www.comsol.com for COMSOL Multiphysics® v. 6.2a, COMSOL AB, Stockholm, Sweden.